Chiral Induction at the Nanoscale and Spin Selectivity in Electron Transmission in Chiral Methylated BEDT-TTF derivatives

Alberta Carella, Suryakant Mishra, Camilla Ferrari, Davide Vanossi, Francesco Rossella, Flavia Pop, Narcis Avarvari, Han Htoon, Jennifer Hollingsworth, Eric Bowes, et al.

Chiral Induction at the Nanoscale and Spin Selectivity in Electron Transmission in Chiral Methylated BEDT-TTF derivatives

Alberta Carella,[1] Suryakant Mishra,[2] Camilla Ferrari,[3] Davide Vanossi,[4] Francesco Rossella,[1] Flavia Pop,[5] Narcis Avarvari,[5*] Han Htoon,[2] Jennifer A. Hollingsworth,[2] Eric G. Bowes,[2] Somak Majumder,[2] Andrew Crandall Jones[2*] and Claudio Fontanesi[3]*

[1]*Department of Physics, FIM, University of Modena and Reggio Emilia, via Campi 213, 41125 Modena, Italy*

[2]*Center for Integrated Nanotechnologies, Los Alamos National Laboratory, Los Alamos, New Mexico, USA*

[3]*Department of Engineering "Enzo Ferrari", (DIEF), Univ. of Modena, Via Vivarelli 10, 41125 Modena, Italy.*

[4]*Department of Chemistry, DSCG, University of Modena and Reggio Emilia, via Campi 183, gg41125, Modena, Italy*

[5]*Univ Angers, CNRS, MOLTECH-Anjou, SFR MATRIX, F-49000 Angers, France.*

ABSTRACT

A great effort has been made in the last decades to realize electronic devices based on organic molecules. A possible approach in this field is to exploit the chirality of organic molecules for the development of spintronic devices, an applicative way to implement the chiral-induced spin selectivity (CISS) effect. In this work we exploit enantiopure Tetrathiafulvalene (TTF) derivatives as chiral inducers at the nanoscale. The aim is to make use of TTF's well-known and unique semiconducting properties, to be expressed in the fields of enantio-selectivity and of chiral-induced spin selectivity (CISS) effect. The experimental results shown in this paper demonstrate further how chirality and spin are deeply interrelated, as foreseen within the CISS effect theory, paving the way to application of TTF derivatives in the field of spintronics. In this work, we demonstrate that tetramethyl-Bis(ethylenedithio)-tetrathiafulvalene (TM-BEDT-TTF) (**1**) behaves as an efficient spin filter, as evidenced by magneto-atomic force microscopy (mc-AFM) measurements. Additionally, it is shown to be effective in transferring chirality to CdS/CdSe core-shell nanoparticles, as inferred from the analysis of circularly resolved photoluminescence spectra. This makes (**1**) a promising candidate for a variety of applications, ranging from plasmonics to quantum computing.

Correspondance
Narcis Avarvari: narcis.avarvari@univ-angers.fr
Andrew Crandall Jones: acj@lanl.gov
Claudio Fontanesi: claudio.fontanesi@unimore.it

1 Introduction

Tetrathiafulvalene (TTF) and its derivatives represent an extensively studied class of electroactive precursors, [1,2] with the objective of the development of molecular conductors and superconductors.[3] Several landmark examples are the first superconducting organic materials pertaining to the Bechgaard family of conductors, [4,5] the TTF-TCNQ charge transfer complex, [6] the high T_c superconductors based on bis(ethylenedithio)-tetrathiafulvalene (BEDT-TTF),[7–9] or many other BEDT-TTF based conductors. [10–13]

More recently, the interest aroused on chiral TTF derivatives, fuelled by the possible intriguing properties of molecular metals featuring handedness.[14] This search for handedness subsequently triggered an intensive endeavour towards the preparation of several families of chiral TTFs.[15–18] Furthermore, chiral TTF derivatives appear as appealing platforms in search of combining their redox-active features with handedness, in electrochemical based studies probing enantioselectivity and chiral induction, [19] in close similarity to the use of thiophene chiral derivatives.[20–23] Since 2011, [24] a continuously increasing activity concerning chiral materials has been dedicated to the investigation of the spin polarization properties through the so-called chirality induced spin selectivity (CISS) effect.[25–29] In this respect, TTF based chiral conductors have allowed the observation of the CISS effect in a BEDT-TTF based chiral superconductor,[30] but also the so-called electrical magnetochiral anisotropy (eMChA) effect in enantiopure dimethyl-ethylenedithio-TTF (DM-EDT-TTF, Scheme 1) based conductors.[31]

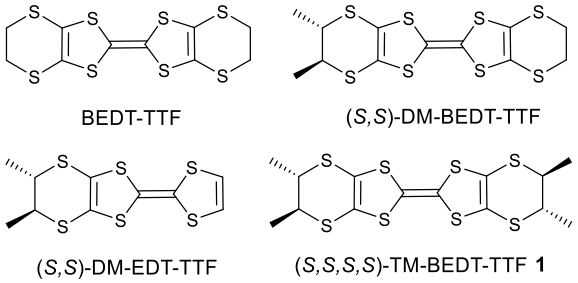

Scheme 1 BEDT-TTF and chiral methylated EDT-TTF and BEDT-TTF donors; only the (*S*) enantiomers are shown. TM-BEDT-TTF **1** was investigated in this work.

Very recently we have evidenced the CISS effect in the methylated BEDT-TTF derivatives DM-BEDT-TTF and TM-BEDT-TTF **1** (Scheme 1, right) through spin-dependent electrochemistry measurements, [32,33] reaching average values of 15% for the spin polarization in the case of the latter. [34]

In this paper we focus on the electronic properties of TM-BEDT-TTF **1,** with particular attention to spin-selective solid-state conduction in its enantiopure pristine state, as well as to the ability to form charge-transfer clusters with CdSe@CdS quantum dots (QD). Magneto conductive atomic force microscopy

(mc-AFM) was carried out on pristine (*S*)-**1** and (*R*)-**1** crystals in the nanometric/micrometric dimension domain, thus envisaging a possible use in solid-state devices as logic gates. Then, chiroptical spectroscopy measurements have been carried out, allowing to detect circularly polarization resolved photoluminescence signals. In practice this can be addressed as circularly polarized photoluminescence (CPL) measurements, the relevant results having been assessed by comparison with semiempirical theoretical calculations (PM6), used to gain a molecular insight in the interaction able to yield chiral-induction in CdSe@CdS QDs adsorbed on top of enantiopure **1** crystals.[25,35,36]

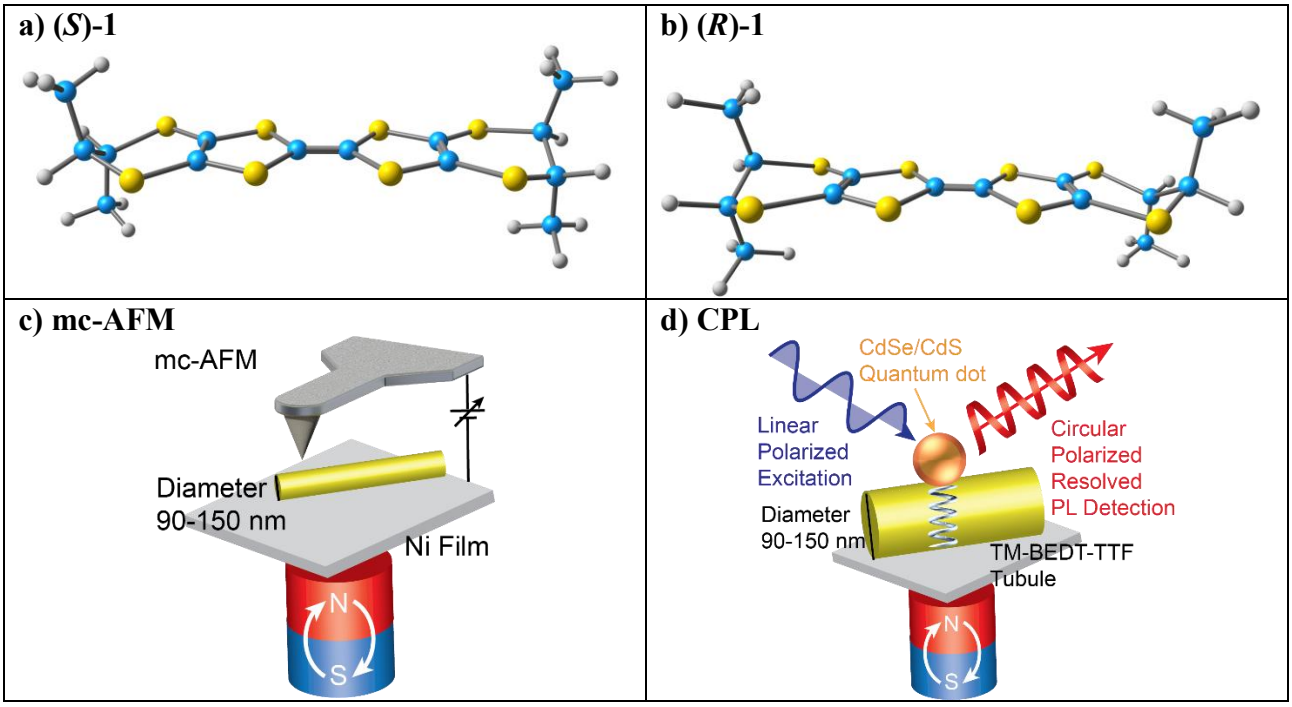

Fig. 1 Ball and stick representation of the molecular structures (colour code used for the atoms are yellow for sulphur, turquoise for carbon and grey for hydrogen): a) (*S*)-**1**; b) (*R*)-**1**. c) mc-AFM experimental setup, helices are meant to represent the enantiopure crystals **1**; d) CPL sample where the sphere represents the QD standing on top of the enantiopure crystal **1**; the substrate is ferromagnetic: nickel.

2. Materials and methods

2.1 Reagents

The synthesis of the Tetramethyl-Bis(ethylenedithio)-Tetrathiafulvalene (TM-BEDT-TTF) enantiomers (*S*)-**1** and (*R*)-**1** has been described in detail in previous papers, and the relevant structures are reported in Figure 1 a&b.[37–39] In electrochemical experiments, tetrabutylammonium tetrafluoroborate (TBATFB) and acetonitrile (ACN) purchased from Merck/SigmaAldrich, have been used as the base electrolyte. A ferrocyanide 5 mM ferricyanide 5 mM in a KCl 0.1 M aqueous solution, referred as the Fe(III)|Fe(II) redox couple, served as a benchmark redox system to probe the surface state of the working electrode. QDs synthesis and stock solution preparation followed exactly the same procedure described in detail

previously.[36] Samples for optical resolved CPL measurements were prepared by dropcasting of a suspension of **1** (0.4mM) in ethanol mixed with a QDs suspension in hexane; additional details are reported in the Supporting Information, Section 1. Samples for mc-AFM were prepared by dropcast of a suspension of **1** (1.5 mM) in ethanol on a Nickel substrate, thus allowing to obtain crystals with a thickness varying between 90 nm and 300 nm. For the Ni substrate, 200nm SiO_2-on-Si (100) wafer substrate was used where 5nm Titanium and 150nm Nickel was deposited in a clean room through electron beam evaporation technique. Additional details about the roughness of Ni substrate are reported in Supporting Information, Section 2.

2.2 mc-AFM

The degree of spin-selective electronic transport was measured on the sample deposited on a nickel substrate using magneto-conductive Atomic Force Microscopy (mc-AFM) Nanosurf Drive and Au-coated AFM probe (spring constant 3 N/m) probes operating in contact mode feedback with the surface. Current vs. potential (*I-V*) curves were collected over a range of -1.5 to 1.5 V using a resistor with R = 10 MΩ and current was measured using a transimpedance amplifier. During the measurements, a magnetic field (0.1 T) was applied either parallel or antiparallel to the surface normal of the Ni substrate using a Nd-Fe-B permanent magnet.

2.3 Photoluminescence experimental setup

A circular polarization resolved optical microscope was used to study the photoluminescence (PL) emission spectrum from single CdSe/CdS QDs. A linearly polarized 405 nm laser with a power of about 5 μW was used to confocally excite individual QDs within the sample was measured using a 50x (NA= 0.9) Olympus objective and routed through a quarter waveplate (QWP) placed on the detection path to project left- ($\sigma-$) and right- ($\sigma+$) circularly polarized PL onto vertical and horizontal polarization directions. A Wollaston prism (1° Separation Angle) was then used before spectrophotometer with liquid nitrogen cooled CCD (Pylon 400BR/Acton SP2300i) to vertically split polarizations and allow simultaneous spectral characterization of the intensity of left- and right-handed polarizations. The polarization anisotropy was determined by analysing the intensity of each polarization. The degree of circular polarization (DCP) was determined as $DCP=(I_1-I_2)/(I_1+I_2)$, where I_1 and I_2 are the photoluminescence intensities of right and left polarization detected on the spectrophotometer after separating them using Wollaston prism. To collect time-resolved PL measurements, the same laser was operated in pulsed mode at a repetition rate of 1 MHz. More details are available in the Supporting Information Section 1.

2.4 Electrochemical setup

Cyclic voltammetry measurements (CV) were performed by using a PGSTAT 128N (Autolab/Metrohm) and CHI660A (CH-Instruments) potentiostats. A typical three-electrode electrochemical cell was employed, where a Pt wire and a silver/silver-chloride (Ag/AgCl/KClsat) electrodes served as the counter (CE) and reference (RE) electrodes, respectively. A 0.1 M tetrabutyl ammonium tetrafluoroborate TBATFB in acetonitrile (ACN) solution was used as base electrolyte. A disk of glassy carbon (GC), or gold, embedded in a teflon cylinder (Metrohm, 3.0 mm diameter) was used as working electrode (WE). All the potentials reported in this work were referred to the Ag/AgCl/KClsat reference electrode. CVs curves of **1** are reported in the Supporting Information, Section 3.

2.5 Circular Dicroism

Circular Dicroism (CD) spectra were recorded using a spectropolarimeter Jasco J-810 in the 200-500 nm wavelength range. Enantiopure solutions of **1** in ACN were measured in a quartz cell of 1 cm, with a scan speed of 100 nm/min, bandwidth and data pitch of 1 nm and response of 1 sec. 10 accumulations were averaged to obtain a reasonable signal-to-noise ratio. CD Spectra are reported in Fig. S4 (Supporting Information, Section 4).

2.6 FT-IR spectra

Grazing angle Fourier transform infra-red, GA-FT-IR, spectra were recorded using a Bruker VERTEX-70 FTIR spectrophotometer equipped with a Globar IR source and a mercury-cadmium-telluride (MCT) Mid-Band detector, in the 4000 – 600 cm^{-1} wavenumber range. 32 scans averaging allowed to obtain a reasonable signal-to-noise ratio. In screening measurements, the angle of the GA accessory was varied in the 80 to 45 degrees, the spectra were recorded with at a 45° angle, please compare Supporting Information, Section 5. Pristine (*S*)-**1** and (*R*)-**1** thick film spectra were measured from thick films obtained by drop-casting a 5 mM solution of enantiopure **1** in DCM on a Pt sheet used both as the mirror for background recording and as the substrate for the drop-casting.

2.7 microRaman spectra

Raman Spectra (for the details please refer to Section 6, Supporting Information) were recorded with a Horiba LabRAM HR Evolution spectrometer coupled to an Olympus BXFM-ILHS microscope equipped with 5X, 10X, 100X, 50X LWD, 100X LWD objectives and diffraction gratings of 600 and 1800 grooves per mm respectively. A 785 nm laser was used with an ND filter of 100% in the 50-1700 cm^{-1} wavenumber range. 5 accumulations of 30 second each averaging allowed to obtain a reasonable signal-to-noise ratio. The ADC detector was set at 45kHz and at -60°C. Pristine (*S*)-**1** and (*R*)-**1**, thick film spectra

were measured from a thick film obtained by drop-casting a 5 mM solution of enantiopure **1** in DCM on a glass sheet.

2.8 Calculation details

Theoretical results here reported refer to calculations performed within the framework of quantum mechanical based programs, by using C1 symmetry and unrestricted wave function, Gaussian[40] and Firefly[41] Rev 8.2026 (Firefly is partially based on the GAMESS (US)8 source code) suite of programs were used. Due to the large Z number of Cd and Se, Hartree-Fock self-consistent field HF-SCF calculations have been carried out at the semi-empirical level of the theory by using the PM6 Hamiltonian. The interaction between QDs and **1** has been simulated generating a Cd16Se16:**1** cluster, the relevant geometrical parameters are obtained by partial-optimization using cartesian coordinates. In particular, the cartesian coordinates of the Cd16Se16 system are kept fixed (constant), corresponding to the geometrical disposition of the cadmium selenide crystal, obtained by X-ray structural analysis in a paper by Freeman et. al.[42] Whilst the intramolecular geometrical parameters of **1**, as well as the distance and orientation of **1** with respect to the Cd16Se16 QD, are fully optimized. Finally, geometry optimization was considered converged when a geometrical search minimization step produced a decrease in energy less then 0.00002 kcal mol^{-1}. Please note that further details concerning theoretical calculations (including optimized cluster cartesian coordinates) are provided in the Supporting Information. The Multiwfn program has been used for visualization and partial elaboration of theoretical results.[43]

3. Results and discussion

3.1 mc-AFM results

Figure 2 shows current vs. potential *(I-V)* curves collected using the magneto conductive atomic force (mc-AFM) setup. Spin-injection is controlled by placing a permanent magnet directly under the Ni substrate, and flipping the orientation, i.e. north or south just in contact with the Ni substrate (as schematically illustrated in Fig. 1c). This experimental setup entailed the recording of *I-V* curves from hundreds of different positions on the crystal surface of **1**, for both out-of and into-plane magnetization directions of the ferromagnetic nickel substrate to control the spin of injected electrons.[22,23,27,36,44] Fig. 2 a&b set out *I-V* curves for (*S*)-**1** and (*R*)-**1** crystals respectively, as a function of the applied magnetic field direction, the crystals being in direct contact with the ferromagnetic nickel surface. In this way the *I-V* curves are representative of the charge transmission through enantiopure crystals of **1** and depend on the spin-injection through the ferromagnetic substrate (i.e., magnetic field UP versus magnetic field DOWN): *I-*

V curves are therefore spin-polarized curves, representative of the charge transport ability as a function of the handedness of **1**.[44] In particular, for (*S*)-**1** the north magnetic field orientation yields the *I-V* curve with the largest current (Fig. 2 a). The opposite is found for the opposite handedness ((*R*)-**1**) as it is shown in Fig. 2 b; indeed, the red curve, south orientation, shows the largest value for the current. Fig. 2c-d show images of the typical (*S*)-**1** and (*R*)-**1** crystal morphology, respectively. *I-V* curves refer to crystals of **1.** The observed diameter of individual fibrils was observed to have representative thicknesses falling in the range of 90 to 150 nm range. While thicker regions of the sample are present, consisting of bundles/aggregates of fibrils, these regions exhibited no measurable current through the nanostructures. CISS characterization was consequently performed on individual fibril nanostructures by performing *I-V* curves over a ±1.5 V range. For these individual fibrils with thicknesses ranging from 90 nm and 150 nm, no significant/systemic variation of CISS effect was observed. For the averaged *I-V* curve, the mean of several hundred of different spatial position on an individual fibril were measured. Moreover, an accurate image analysis allows to detect the **1** handedness. The quantitative analysis of mc-AFM *I-V* curves shown in Fig. 2a-b as a function of the magnet orientation allows to calculate a spin-polarization value ranging between 40% and 50%, for a ±1.5 V bias.

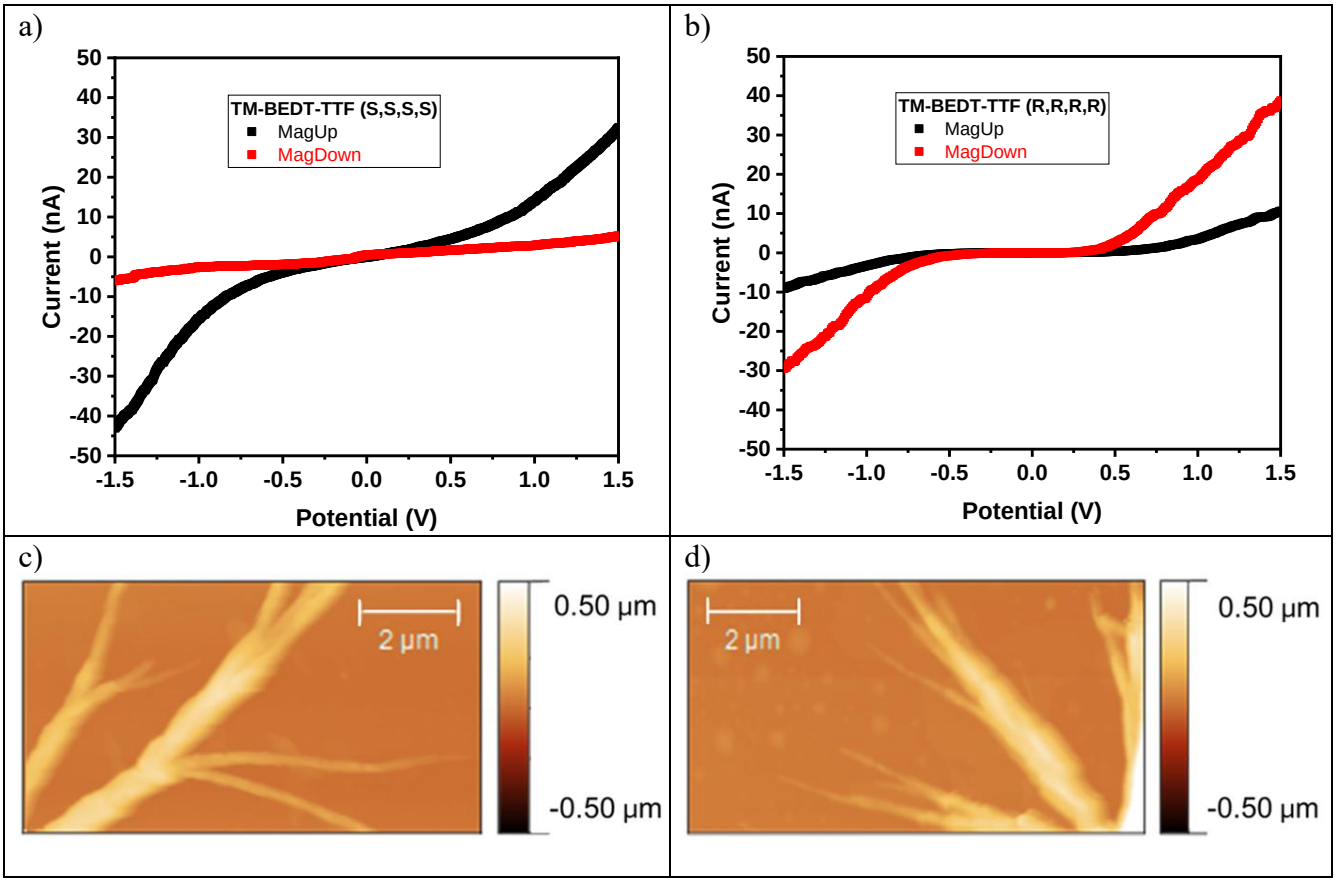

Fig. 2 Magneto conductive AFM, mc-AFM, experimental *I-V* curves in the -1.5 V to +1.5 V potential range, AFM images of **1** crystal morphology. The experimental mc-AFM setup is schematized in Figure 1c. *I-V* curves a) (*S*)-**1** and b) (*R*)-**1**. Spin-selective transport is detected, with spin polarization values in the 30% to 50% range, see the text for a detailed discussion. Two typical examples of topographic maps of c) (*S*)-**1** and d) (*R*)-**1** crystals.

3.2 Chiral induced CPL

A suspension of crystals of **1** was prepared in ethanol and mixed by ultrasonication with a hexane suspension of CdSe@CdS quantum dots (QDs). The final suspension was then drop-casted on a clean Ni(150 nm)/Ti(5 nm) surface. To probe the ability of **1** as chiral inducer, colloidal CdSe/CdS core/shell QDs were employed as the quantum light emitter. QDs were uniformly spin casted from a suspension of crystals of **1** mixed with the QDs suspension in hexane from a dilute solution. The whole procedure is reported in detail in the Supporting Information, Section 1. QD light emitters were photoexcited above the relevant bandgap by using a pulsed laser source operating at ~3 eV (405 nm). QDs individual emitters were spotted exploiting widefield illumination imaging. Fig. 3 shows circular-polarization resolved QDs PL spectra recorded in the 590 to 720 nm range. Fig. 3a sets out the spectra of the QD: (*S*)-**1** system. Remarkably, the signal relevant to the left-handed (σ^-) polarized photoluminescence (red curve) is larger than that of the right-handed (σ^+) polarization, this result being in agreement with the sign of the CD spectrum of (*S*)-**1** (reported in Fig. S4 of the Supporting Information). Fig. 3b sets out the PL results for the QD:(*R*)-**1** system following exactly the same experimental procedure, the opposite pattern being obtained, that is the signal relevant to the right-handed (σ^+) polarized photoluminescence (black curve) is larger than that of the left-handed (σ^-) polarization. Analysis of the circular polarized PL spectra allowed the determination of the degree of circular polarization (DCP) of photoluminescence to be 15% DCP, calculated from the PL curves shown in Fig. 3. Chiral induction of **1** on QDs can be explained by the possible formation of a quasi-chemical interaction between the enantiopure **1** and the cadmium selenide QD, as it is discussed in detail on the basis of theoretical results (*vide infra*). Remarkably, these experimental observations are consistent with previous reports showing dichroic signals, in PL active achiral systems, following chiral induction.[36]

a) QD:(*S*)-**1**	b) QD:(*R*)-**1**

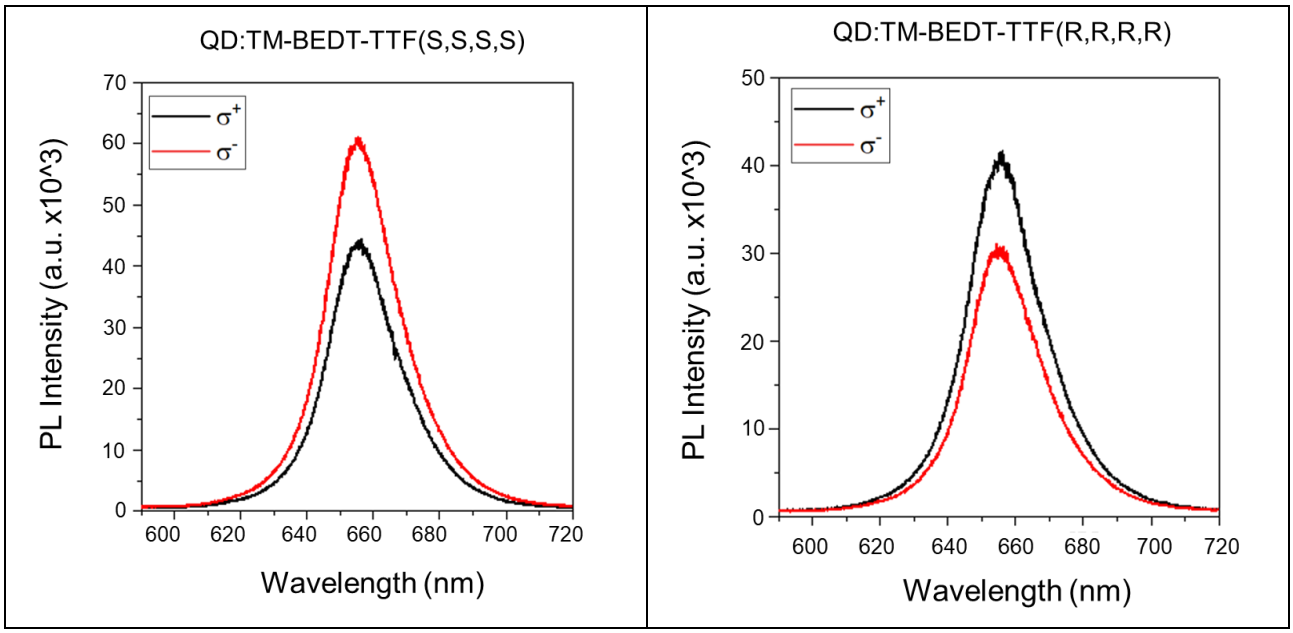

Fig. 3 Circular Polarization resolved PL spectra. a) QD:(*S*)-**1** b) QD:(*R*)-**1**.

3.3 Theoretical modelling

The interpretation of degree of circular polarization detected in photoluminescence spectra (experimental circular polarization resolved PL spectra in Figure 3) necessarily goes through the use of quantum mechanical (QM) based modelling of the QD:**1** system. and requires a number of approximations and methodological choices.

Modelling of the interaction of (*S*)-**1** and (*R*)-**1** with the QDs is not a trivial task, since both Cd and Se are heavy elements where the combination of electron numbers and the need to account for relativistic effects virtually impede the use of an all-electron ab-initio theoretical approach. This in addition to the issue of the large number of atoms of the QD:**1** cluster.

Approximations underlying the choice of both the quantum-mechanical level of the theory and the assembling of the QD:**1** cluster geometry and optimization, in short are as follows:

1. The semiempirical Hamiltonian, PM6, is used in cluster geometry optimization.
2. The QD:**1** cluster (please note that the cluster is indicated as QD:**1**, indicating both (*S*)-**1** or (*R*)-**1**, the two different enantiomers would yield exactly the same theoretical result in that the CdSe slab is achiral). is modelled using a Cd16Se16 slab whose relevant geometrical coordinates are kept constant to those of the experimental crystal, Figure S9.[42]

3. the selection of the proper excited state electronic nature (i.e. spin-multiplicity) is a key-factor in the theoretical modelling of the luminescence spectra. Comparison limited to the triplet and quintet excited states show that the triplet is more stable than the quintet by about 15 kcal mol^{-1}.

Much more details concerning the procedure followed in theoretical calculations are provided in the Supporting Information, Section 7. This together with the $Cd_{16}Se_{16}$-(*S*)-**1** cartesian coordinates of the singlet, triplet and quintet electronic states, obtained by PM6 partial optimization.

*3.3.1 The QD:**1** cluster geometry*

The modelling of QD:**1** cluster interactions and electronic properties has been carried out considering a single molecule interacting with a Cd16Se16 slab, as it is schematically represented in Fig. 4a for the $Cd_{16}Se_{16}$:(*S*)-**1**. As outlined above in point 2, the theoretical geometry optimization of the cluster is carried out with the parameters of the cadmium selenide slab kept fixed (it is a solid), the Cd16Se16 slab coordinates correspond to those of the CdSe crystal.[42] Theoretical results suggests that the QD:**1** cluster is characterized by a pronounced stability. In that, the QD:**1** cluster formation energy (E_{C-F}, equation 1) is found to be $-19.5\ kcal\ mol^{-1}$, in the case of the ground state singlet electronic state.

$$E_{C-F} = E_{\mathrm{QD:}\mathbf{1}\ cluster} - (E_{Cd16Se16} - E_{\mathbf{1}}) \quad (1)$$

Where: E_{C-F} is the cluster formation energy, $E_{\mathrm{QD:}\mathbf{1}\ cluster}, E_{Cd16Se16}, E_{\mathbf{1}}$ are the QD:**1** cluster, $Cd_{16}Se_{16}$ slab and **1** energies, respectively. In the calculations, energies are to be intended as the self-consistent total electronic energy values. Thus, the interaction between **1** with the cadmium selenide slab is found down-hill in energy, and large enough to be able to drive the adsorption of the QD on top of the organic crystals. As it can be seen by analysis of the distances between **1** and the QD (see Figure S10a, Supporting Information), the bonding interaction between the 1 and QD is mainly driven by the strong interaction between the sulphur atoms present in the (*S*)-1 molecule and the cadmium. As it can be also noted comparing the frontier orbitals energy for the pristine Cd16Se16 slab and 1 compared with that of the cluster, the latter HOMO/LUMO energy difference is definitely quite smaller as shown in Figure 4b. The optimized sulphur−cadmium distance is found in the 2.6 to 2.9 Å range. The latter results are consistent with structural data of the cadmium sulphide crystal featuring an experimental formation enthalpy of $-38.6\ kcal\ mol^{-1}$ and a sulphur−cadmium distance of 2.55 Å. Thus, PM6 calculated cadmium−sulphur (sulphur atoms of **1**) geometrical distances and E_{C-F} values compare well with the experimental results of the bulk CdSe crystal. [45]

3.3.2 Theoretical calculation of photoluminescence spectra

Analysis of the electronic density, as implemented within the Mulliken framework, shows that there is a rather larger charge transfer from the CdSe slab towards the **1** molecule of 0.39 electrons in the singlet electronic state. Interestingly, a significantly larger charge transfer of 0.59 electrons is calculated for the QD:**1** triplet electronic state, which is the state assumed to yield photoluminescence after suitable photo-excitation. The $Cd_{16}Se_{16}$:(*S*)-**1** quintet excited state is calculated to lay 50.5 $kcal\ mol^{-1}$ (2.17 eV) higher in energy with respect to the triplet (compare Figure S9b and the cartesian coordinates reported in the Supporting Information, Section 7). Calculated emission TD electronic spectra of the QD:**1** cluster, triplet state, show a significant intensity in the window centred at 650 nm, with also an associated large optical activity, whose sign depends on the handedness of **1**. The relevant calculated circular polarization strength *vs* wavelength CD spectra are shown in Fig. 4c. The theoretical outcome here outlined is in general agreement with previous results already reported in the literature.[46–48]

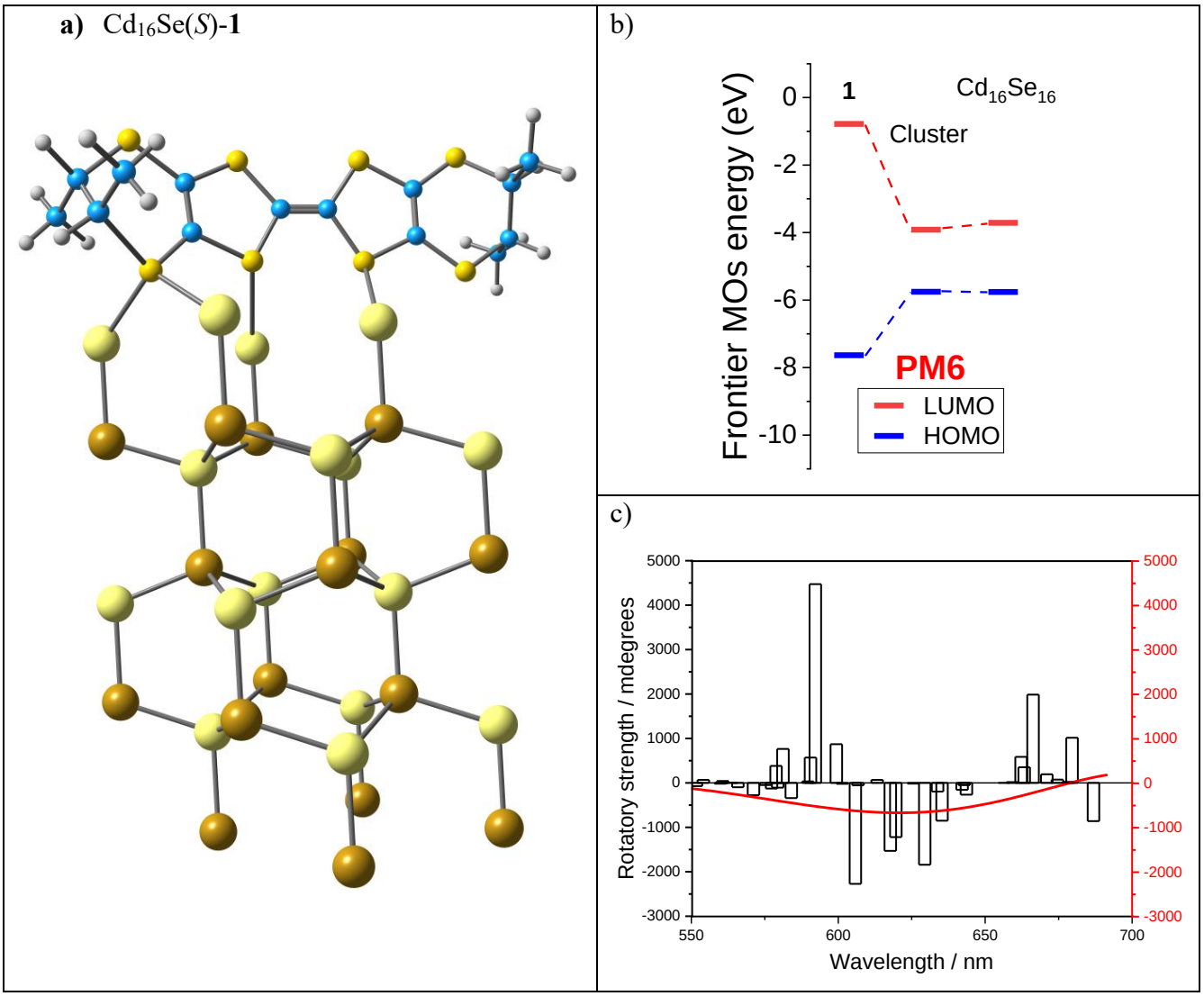

Fig. 4 a) $Cd_{16}Se_{16}$: (*S*)-**1** cluster molecular structure; colour code used for the atoms is yellow for sulphur, turquoise for carbon, grey for hydrogen, bright yellow larger sphere for cadmium and brown larger sphere for selenium. b) CD emission (luminescence), rotational strength spectrum of $Cd_{16}Se_{16}$:(*S*)-**1** from the triplet state, in the 550 to 700 nm window: black bars represent the transition numerical rotational strength, the red line is the Gaussian broadening with band width at half height of 150 nm (Figure S11, Supporting Information, reports the spectrum in the broader 300 to 1500 nm range. Are also shown the shape of molecular orbitals featuring the largest weight in the 635.0 nm electronic transition, Figure S12). c) MOs correlation diagram, the frontier energies of the **1**, $Cd_{16}Se_{16}$ and $Cd_{16}Se_{16}$:**1** molecular species are reported. PM6 level of the theory.

4. Conclusions

This study focuses on the relationship between spin and handedness as the subject of investigation, trying to shed further light on the chiral-induced spin selectivity (CISS) effect.[26] Accordingly, consistent data have been obtained investigating crystals featuring opposite handedness of tetramethyl BEDT-TTF (TM-

BEDT-TTF) derivatives, where mc-AFM and CPL measurements show a clear interplay in between spin-polarization and handedness. In particular three specific points are worth to be remarked.

Spin-selective transport and chiroptical properties of enantiomers of TM-BEDT-TTF **1** have been studied in detail.

The mc-AFM *I-V* curves of crystals of **1** show a notable semi-conductive character,[38] which is also associated with a significative spin-selectivity ability. SP% is found in the 30% and 50% range, thus giving indication of the possible use of **1** for the practical implementation of spin-gate in solid-state devices.

Circular polarization resolved PL spectra indicate the occurrence of a strong chiral-induction effect of **1**, suggesting a significant interaction between **1** and the $Cd_{16}Se_{16}$ slab. Experimentally, this intermolecular interaction yields circular polarization in the luminescence spectra, thus indicating a strong chiral induction of **1**. This paves the way towards the possible use in optoelectronic devices whose light emitting characteristics, in particular polarized emission, can be suitably tailored by coupling chiral TTF derivatives such as **1** with QDs.

Conflicts of interest
There are no conflicts of interest to declare.

Acknowledgements
Financial support is gratefully acknowledged from the Ministry of University and Research (MUR), PRIN 2022 cod. 2022NW4P2T "From metal nanoparticles to molecular complexes in electrocatalysis for green hydrogen evolution and simultaneous fine chemicals production (FUTURO)", PI Dr. Francesco Vizza, from Fondazione di Modena, Fondo di Ateneo per la Ricerca Anno 2023, linea FOMO, Progetto AMNESIA and from Consorzio Interuniversitario Nazionale per la Scienza e Tecnologia dei Materiali (INSTM), fondi triennali: "INSTM21MOFONTANESI". This work was supported in France by the CNRS, the University of Angers and the French National Agency for Research (ANR) project SECRETS (ANR PRC 20-CE06-0023-01). C.F. gratefully acknowledges Los Alamos National Lab Project: 2024AC0022, SONG: Spin rOle iN charGe transfer @ 2D chiralized interfaces. Work was conducted in part at the Center for Integrated Nanotechnologies (CINT), a Nanoscale Science Research Center and User Facility operated for the U.S. Department of Energy (DOE), Office of Science (SC), Office of Basic Energy Sciences (BES). S. M. acknowledges support from a Laboratory Directed Research and Development (LDRD) Director's Postdoctoral fellowship 20230854PRD2. A.C.J., H. H. and J.A.H. acknowledge support from the LDRD Directed Research program 20220047DR. A.C.J acknowledges further support by 20230347ER. E.G.B. was funded by CINT. A.C. and F.R. gratefully acknowledge financial support from the European Union-Next Generation funds through Centro Nazionale per la Mobilità Sostenibile (CNMS), Mission 4, Spoke 13, CN_4 Project (CUP E93C22001070001).

References

1 J. Yamada and T. Sugimoto, *TTF Chemistry: Fundamentals and Applications of Tetrathiafulvalene*, Kodansha Ltd: Tokyo and Springer-Verlag: Berlin, Heidelberg, New York., 2004.
2 F. Pop and N. Avarvari, *Chem. Commun.*, 2016, **52**, 7906–7927.
3 T. Ishiguro, K. Yamaji and G. Saito, *Organic Superconductors*, Springer, Berlin, Heidelberg, 1998, vol. 88.
4 D. Jérome, A. Mazaud, M. Ribault and K. Bechgaard, *J. Phyique Lett.*, 1980, **41**, 95–98.
5 K. Bechgaard, K. Carneiro, F. B. Rasmussen, M. Olsen, G. Rindorf, C. S. Jacobsen, H. J. Pedersen and J. C. Scott, *J. Am. Chem. Soc.*, 1981, **103**, 2440–2442.
6 John. Ferraris, D. O. Cowan, V. Walatka and J. H. Perlstein, *J. Am. Chem. Soc.*, 1973, **95**, 948–949.
7 H. Urayama, H. Yamochi, G. Saito, K. Nozawa, T. Sugano, M. Kinoshita, S. Sato, K. Oshima, A. Kawamoto and J. Tanaka, *Chemistry Letters*, 1988, **17**, 55–58.
8 K. Miyagawa, K. Kanoda and A. Kawamoto, *Chem. Rev.*, 2004, **104**, 5635–5654.
9 A. M. Kini, U. Geiser, H. H. Wang, K. D. Carlson, J. M. Williams, W. K. Kwok, K. G. Vandervoort, J. E. Thompson and D. L. Stupka, *Inorg. Chem.*, 1990, **29**, 2555–2557.
10 H. Kobayashi, R. Kato, T. Mori, A. Kobayashi, Y. Sasaki, G. Saito and H. Inokuchi, *Chemistry Letters*, 1983, **12**, 759–762.
11 T. Mori, *Chem. Rev.*, 2004, **104**, 4947–4970.
12 E. Coronado and P. Day, *Chem. Rev.*, 2004, **104**, 5419–5448.
13 M. Allain, C. Mézière, P. Auban-Senzier and N. Avarvari, *Crystals*, 2021, **11**, 386.
14 F. Pop, N. Zigon and N. Avarvari, *Chem. Rev.*, 2019, **119**, 8435–8478.
15 J. D. Wallis and J.-P. Griffiths, *J. Mater. Chem.*, 2005, **15**, 347–365.
16 N. Avarvari and J. D. Wallis, *J. Mater. Chem.*, 2009, **19**, 4061–4076.
17 A. Bogdan, I.-T. Moraru, P. Auban-Senzier, I. Grosu, F. Pop and N. Avarvari, *Molecules*, 2022, **27**, 6926.
18 N. Mroweh, T. Cauchy, N. Vanthuyne and N. Avarvari, *CrystEngComm*, 2022, **24**, 6187–6197.
19 C. Ferrari, A. Bogdan, F. Pop, C. Curto, A. Carella, F. Rossella, N. Avarvari and C. Fontanesi, *Chirality*.
20 S. Grecchi, C. Ferdeghini, M. Longhi, A. Mezzetta, L. Guazzelli, S. Khawthong, F. Arduini, C. Chiappe, A. Iuliano and P. R. Mussini, *ChemElectroChem*, 2021, **8**, 1377–1387.
21 S. Grecchi, S. Arnaboldi, S. Rizzo and P. R. Mussini, *Current Opinion in Electrochemistry*, 2021, **30**, 100810.
22 A. Stefani, M. Innocenti, W. Giurlani, N. Calisi, M. Pedio, R. Felici, L. Favaretto, M. Melucci, C. Zanardi, A. C. Jones, S. Mishra, N. Zema and C. Fontanesi, *The Journal of Chemical Physics*, 2023, **159**, 104701.
23 A. Stefani, T. Salzillo, P. R. Mussini, T. Benincori, M. Innocenti, L. Pasquali, A. C. Jones, S. Mishra and C. Fontanesi, *Advanced Functional Materials*, 2024, **34**, 2308948.
24 B. Gohler, V. Hamelbeck, T. Z. Markus, M. Kettner, G. F. Hanne, Z. Vager, R. Naaman and H. Zacharias, *Science*, 2011, **331**, 894–897.
25 D. Di Nuzzo, C. Kulkarni, B. Zhao, E. Smolinsky, F. Tassinari, S. C. J. Meskers, R. Naaman, E. W. Meijer and R. H. Friend, *ACS Nano*, 2017, **11**, 12713–12722.
26 R. Naaman, Y. Paltiel and D. H. Waldeck, *Nature Reviews Chemistry*, 2019, **3**, 250.
27 C. Fontanesi, E. Capua, Y. Paltiel, D. H. Waldeck and R. Naaman, *Advanced Materials*, 2018, **30**, 1707390.
28 H. Lu, J. Wang, C. Xiao, X. Pan, X. Chen, R. Brunecky, J. J. Berry, K. Zhu, M. C. Beard and Z. V. Vardeny, *Science Advances*, 2019, **5**, eaay0571.
29 B. P. Bloom, Y. Paltiel, R. Naaman and D. H. Waldeck, *Chem. Rev.*, 2024, **124**, 1950–1991.

30 R. Nakajima, D. Hirobe, G. Kawaguchi, Y. Nabei, T. Sato, T. Narushima, H. Okamoto and H. M. Yamamoto, *Nature*, 2023, **613**, 479–484.
31 F. Pop, P. Auban-Senzier, E. Canadell, G. L. J. A. Rikken and N. Avarvari, *Nat Commun*, 2014, **5**, 3757.
32 C. Fontanesi, *Current Opinion in Electrochemistry*, 2018, **7**, 36–41.
33 P. C. Mondal, V. Singh and M. Zharnikov, *Acc. Chem. Res.*, 2017, **50**, 2128–2138.
34 A. Stefani, A. Bogdan, F. Pop, F. Tassinari, L. Pasquali, C. Fontanesi and N. Avarvari, *The Journal of Chemical Physics*, 2023, **159**, 204706.
35 D. Di Nuzzo, L. Cui, J. L. Greenfield, B. Zhao, R. H. Friend and S. C. J. Meskers, *ACS Nano*, 2020, **14**, 7610–7616.
36 S. Mishra, E. G. Bowes, S. Majumder, J. A. Hollingsworth, H. Htoon and A. C. Jones, *ACS Nano*, 2024, **18**, 8663–8672.
37 J. D. Wallis, A. Karrer and J. D. Dunitz, *Helvetica Chimica Acta*, 1986, **69**, 69–70.
38 F. Pop, S. Laroussi, T. Cauchy, C. J. Gomez-Garcia, J. D. Wallis and N. Avarvari, *Chirality*, 2013, **25**, 466–474.
39 S. Yang, F. Pop, C. Melan, A. C. Brooks, L. Martin, P. Horton, P. Auban-Senzier, G. L. J. A. Rikken, N. Avarvari and J. D. Wallis, *CrystEngComm*, 2014, **16**, 3906–3916.
40 J. A. Pople, Gaussian suite of programs http://gaussian.com/ 2017.
41 M. W. Schmidt, K. K. Baldridge, J. A. Boatz, S. T. Elbert, M. S. Gordon, J. H. Jensen, S. Koseki, N. Matsunaga, K. A. Nguyen, S. Su, T. L. Windus, M. Dupuis and J. A. Montgomery, *Journal of Computational Chemistry*, 1993, **14**, 1347–1363.
42 D. K. Freeman, S. L. Mair and Z. Barnea, *Acta Crystallographica Section A*, 1977, **33**, 355–359.
43 T. Lu and F. Chen, *Journal of Computational Chemistry*, 2012, **33**, 580–592.
44 F. Tassinari, D. R. Jayarathna, N. Kantor-Uriel, K. L. Davis, V. Varade, C. Achim and R. Naaman, *Advanced Materials*, 2018, **30**, 1706423.
45 S. S. Zumdahl, *Chemical Principles 6th Ed. Houghton Mifflin Company.*, Houghton Mifflin Company, 2009.
46 S. Naskar, V. Mujica and C. Herrmann, *J. Phys. Chem. Lett.*, 2023, **14**, 694–701.
47 M. S. Zöllner, S. Varela, E. Medina, V. Mujica and C. Herrmann, *J. Chem. Theory Comput.*, 2020, **16**, 2914–2929.
48 M. S. Zöllner, A. Saghatchi, V. Mujica and C. Herrmann, *J. Chem. Theory Comput.*, 2020, **16**, 7357–7371.